ICAS 2020 SHANGHAI
International Council of the Aeronautical Sciences
32nd Congress of the International Council of the Aeronautical Sciences
September 6-10, 2021
Pudong Shangri-La, Shanghai, China

DEVELOPMENTS TOWARDS A TOOLCHAIN FOR UAV FLIGHT DYNAMIC MODELS IN EARLY DESIGN

Sebastian J. Koeberle[1] & Mirko Hornung[1]

[1]Institute of Aircraft Design, Technical University of Munich, Germany

Abstract

Unmanned, subscale technology demonstrators have gained interest as research platforms in the recent years due to their cost saving potential in comparison to manned aircraft and versatility. The customization of technology demonstrators to research purposes often leads to specialized configurations that elude conventional design rules, which has lead to undesirable dynamic characteristics in the past. In order to factor the dynamic characteristics into the design process during its early stages, approaches to predict the aerodynamic coefficients involved in the Short Period mode of an unmanned aircraft based on elementary design data are investigated. Three different methods, based on geometric relations and the vortex-lattice simulation program *Athena Vortex Lattice 3.37*, are presented, calculations conducted and resulting estimations compared to values identified from flight test data. Results show the feasibility of predicting the frequency and damping of the Short Period mode as well as the influencing aerodynamic coefficients based on elementary design data. In terms of prediction accuracy concerning the aerodynamic coefficients, large differences were found: For the coefficients related to the lift slope and pitch rate induced moment, predicted values were found to be within the 95%-confidence interval of the identified values. The predicted coefficient for aerodynamic pitching moment, however, ranged from 75% to more than 200% of the identified value. These results indicate the necessity to account for aerodynamic effects caused by the fuselage.

Keywords: Unmanned Aerial Vehicles, System Identification, Flight Testing, Aircraft Design

1. The Design of Unmanned Technology Demonstrators.

The use of unmanned, subscale demonstrators for technology demonstration in flight has increased over the past years [1], as it bears the advantage of cost savings as compared to the use of manned test beds and can open a different range of possible flight experiments. In the case of the FLEXOP flight demonstrator, which is employed for testing load alleviation and flutter suppression technologies in flight, some test points beyond the open-loop flutter boundary are considered too risky to be conducted on a manned test bed [2]. While being largely influenced by model aircraft technology [2, 3], the design of such demonstrators has to comply with a wide range of technological and legislative requirements that often lead to specialized configurations that elude conventional design rules [4]. In the past, this has lead to unfavorable characteristics, such as high workload for external pilots, increased trim drag, or hindered go-around capabilities, which shifts the focus towards the necessity to consider flying qualities early in the design, in order to facilitate operation in the future.

For manned aircraft, research concerning the consideration of flying qualities in early design phase has been conducted already: The design tool *AeroMech* is described by Chudoba [5] that aims at the consideration and design of control effectors in conceptual design in order to assure advantageous flying qualities and mitigate related design risks. Sorajini et al. have published on the *Dynamic Environment for Loads Prediction and Handling Investigation* (DELPHI) that allows the definition of a wide range of aircraft and the simulation of maneuvers with the purpose of being a key enabler of simulation-assisted certification and design [6]. The authors stress the necessity to employ inputs in a wide range of fidelity: As the design process unfolds, more and more information in increasing level of detail becomes available, refining the results and accuracy of the implemented simulation.

In the domain of recreational, remote-controlled sailplanes, Quabeck has presented a conclusive handbook method for the design of sailplanes with a focus on flight dynamics, including in terms of damping coefficients for pitching, yawing and rolling motion [7, 8]. In this field, the methods distinguish themselves by a sound theoretical foundation that is implemented into pragmatic design relations.
Once the dynamic characteristics of a new design are available, the problem of evaluating them in terms of handling qualities arises: As handling qualities profoundly shape the interaction between aircraft and human pilot, the Cooper-Harper Scale focuses on pilots' ratings for evaluation of handling qualities [9]. A similar approach could be applicable to unmanned aerial vehicles (UAVs) and external pilots who often argue that different UAVs "feel" different, even if only visual feedback is available [10]. This approach, however, has the disadvantages that a high number of external pilots has to be surveyed on a high number of UAVs in order to derive conclusions which then might not be applicable for the external pilot at hand. Offering a more analytical approach, methods employing eigenvector similitude [11] or frequency response analysis [12] have been proposed. Using these methods, it is possible to compare the dynamic characteristics of a new design to the dynamic characteristics of a well-tested design which flying qualities are deemed desirable.
In order to predict the flight dynamics characteristics of unmanned aircraft in early design stage, the goal of this study is to identify driving influences in order to assure benign operational characteristics in future designs. Especially the longitudinal motion has been identified to pose the most prominent problem in this regard, specifically if the frequency and damping of the Short Period mode are so low, that the coupling into the Phugoid mode starts to cause tangible effects. Therefore, an investigation will be undertaken to estimate the relevant parameters of the Short Period mode based on data typically available during the early stages of a design process and results subsequently compared to flight test data.
In the upcoming chapters the DG-800 S flying testbed, that serves as a case study, is showcased, an overview over the flight tests conducted and its results given, as well as the method of design data acquisition described. Methods for estimating the longitudinal dynamics are presented and results discussed. In the appendix, a condensed summary of the handbook methods, the nomenclature as well as the geometric data used is given.

2. The DG-800 S Flying Testbed

In order to create a data base, flight tests have been conducted in summer 2020 using a *CARF-Models Ltd.* DG-800 S [4, 13] as a flying testbed. The UAV is depicted in Fig. 1, technical data listed in Table 1. It features a variety of sensors for data collection and operation that are integrated in the available space below the orange cockpit hatch [14, 15]. Flight test results included parame-

Figure 1 – Instrumented UAV *CARF-Models Ltd.* DG-800 S on the runway (picture courtesy of Lars H. Nagel).

ter estimations from a total of 30 test points to identify the parameters of Short Period mode (nine testpoints), Dutch Roll (eleven testpoints) and Roll mode (ten testpoints) [4] at airspeeds V between airspeed $V = 28\frac{m}{s}$ and airspeed $V = 62\frac{m}{s}$, thus a range where linear aerodynamics can be assumed. For each testpoint considered, the poles of the respective eigenmode have been identified. The resulting pole-zero map is given in Fig. 2, note the different scaling of the y-axis in the left and the more detailed right plot. The overall position of poles is plausible, even though considerable scatter is exhibited in the case of the poles of the Short Period mode. Each testpoint was used to identify

the related aerodynamic coefficients, which values were subsequently averaged over the number of testpoints. The resulting coefficient estimates for the Short Period Mode are summarized in Table 2.

Table 1 – Technical data of the UAV *CARF-Models Ltd.* DG-800 S.

Wing Span	$6\ m$	Take-off Weight	ca. $20.3\ kg$
Wing Area	ca. $1.3\ m^2$	Flight Time	ca. 8 minutes
Length	$2.35\ m$	Max. Thrust	$100\ N$ [16]
RC-Functions	Ailerons, Flaps, Rudder, Elevator, Spoiler, Throttle, Gear		
	Switch for experiments power supply		

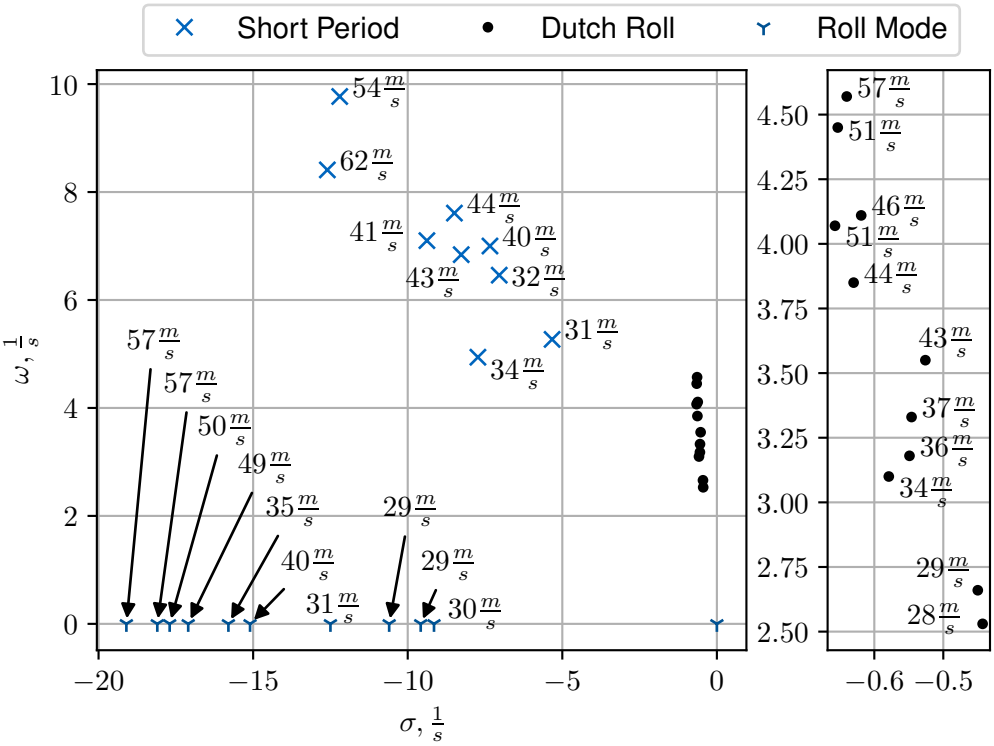

Figure 2 – Pole-Zero Plot resulting from the parameter identification of each test point of the fligh tests conducted in summer 2020, annotated with the respective rounded value of trimmed airspeed V_0 [17].

Table 2 – Averaged aerodynamic coefficients and standard deviations $s_{[\,]}$ involved in the Short Period mode [4], differing values due to adjusted reference length/area.

$C_{L\alpha}+C_{D\|0}$	6.5782	$C_{m\alpha}$	-0.5143	C_{mq}	-21.7515
$s_{C_{L\alpha}+C_{D\|0}}$	0.7825	$s_{C_{m\alpha}}$	0.1377	$s_{C_{mq}}$	6.3079

In order to collect the data necessary for simulation a combined approach of researching freely available information and elaborate analysis of 3D-scanning data has been chosen. The *CARF-Models Ltd.* DG-800 S [13] is a 1:3 scale version of the *Glaser-Dirks DG-800 S*, therefore available data of both the model and the full-scale aircraft were researched.
A more elaborate process using 3D-scan data was employed in order to attain geometric design data of the DG-800 S, especially concerning the cross-sections/airfoils of aerodynamic surfaces. An optical coordinate measuring system of type *Creaform Maxshot 3D* [18] and a 3D-scanner of type *Creaform HandyScan 3D* [19] was used to collect 3D-scan data. The first scanning device is used

to create a reference system featuring deviations as little as 0.005 $\frac{mm}{m}$ and a volumetric accuracy of up to 0.015 $\frac{mm}{m}$. The second scanning system uses the created reference system to orient itself in space and takes 3D measurements of surfaces with a volumetric accuracy of 0.020 mm+0.015 $\frac{mm}{m}$. The resulting 3D-scan data is subsequently analyzed, for which two tools are available: The propriety software *Creaform VX-elements* [20] and a custom toolchain, specifically developed to extract geometric information from 3D-scan data of UAVs for the purpose of aerodynamic simulation [21, 22]. *VX-elements* is a comprehensive software suite supplied with aforementioned 3D-scanners comprising software solutions for scanning, inspecting and preparing of 3D-scan data for subsequent use in computer aided design software. It is used to attain the overall measures of the UAV and for creating cross-sections of the fuselage. In order to extract geometric information of the wings, custom made software is deployed. The toolchain orients the aircraft in space, slices the aerodynamic surfaces in predefined locations and interpolates the resulting points. The emerging airfoils have been shown to represent the original airfoils sufficiently closely for the intended simulation purpose, both in geometric and aerodynamic properties [22].
Throughout the process of compiling the data necessary for subsequent simulation, data from different sources were compared and cross-checked.

3. Methods of Estimation of Longitudinal Dynamics

In this chapter, an overview over the theories and methods employed is given. Firstly a theoretical description of the Longitudinal equations of motion in terms of a state-space model is described. Secondly two methods for the estimation of frequency and damping of the Short Period mode are presented, namely aforementioned handbook method by Dr. Helmut Quabeck [7, 8] as well as the program *Athena Vortex Lattice* by Mark Drela and Harold Youngren [23]. In terms of notation, symbols are adopted as presented in the primary sources.

3.1 Longitudinal Dynamics of an Aircraft

For the description of the longitudinal motion, the following linearized state-space model is used, accepting inaccuracies introduced by neglecting the coupling between lateral and longitudinal motion, as well as forces in x- and z-direction due to the pitch rate q [4, 24].

$$\begin{bmatrix} \dot{V} \\ \dot{\gamma} \\ \dot{\alpha} \\ \dot{q} \end{bmatrix} = \begin{bmatrix} X_V & -g & X_\alpha - g & 0 \\ -Z_V & 0 & -Z_\alpha & 0 \\ Z_V & 0 & Z_\alpha & 1 \\ M_V & 0 & M_\alpha & M_q \end{bmatrix} \cdot \begin{bmatrix} V \\ \gamma \\ \alpha \\ q \end{bmatrix} + \begin{bmatrix} X_\eta & N_{\delta_T} \\ -Z_\eta & -Z_{\delta_T} \\ Z_\eta & Z_{\delta_T} \\ M_\eta & M_{\delta_T} \end{bmatrix} \cdot \begin{bmatrix} \eta \\ \delta_T \end{bmatrix} \tag{1}$$

Assessing equ. 1 it gets apparent, that the Short Period mode, which is dominated by the angle of attack α combined with pitch rate q, and the Phyoid, which is dominated by the airspeed V and flight path angle γ, are coupled by the state-space parameters Z_V, M_V, and Z_α. In order to decouple the Short Period mode from the Phugoid, the terms Z_V and M_V can be set to 0 in a first approximation [24]. Thus, the state-space model describing the Short Period mode can be further simplified to

$$\begin{bmatrix} \dot{\alpha} \\ \dot{q} \end{bmatrix} = \begin{bmatrix} Z_\alpha & 1 \\ M_\alpha & M_q \end{bmatrix} \cdot \begin{bmatrix} \alpha \\ q \end{bmatrix} + \begin{bmatrix} Z_\eta \\ M_\eta \end{bmatrix} \cdot \begin{bmatrix} \eta \end{bmatrix} \tag{2}$$

From equ. 2 the characteristic polynomial is derived that leads to the following approximations for the eigen-frequency $\omega_{0,SP}$, damping σ_{SP}, and frequency ω_{SP} of the Short Period mode by comparison of coefficients:

$$s^2 - s(M_q + Z_\alpha) + M_q Z_\alpha - M_\alpha = 0 \tag{3}$$

$$\omega_{0,SP} \approx \sqrt{Z_\alpha M_q - M_\alpha} \tag{4}$$

$$\sigma_{SP} \approx \frac{1}{2}(M_q + Z_\alpha) \tag{5}$$

$$\omega_{SP} = \sqrt{\omega_{0,SP}^2 - \sigma_{SP}^2} \tag{6}$$

The state space parameters can be calculated using the following relations. Note, that in case of the parameter M_q in equ. 8, the pitch rate q is de-dimensionalized using the factor $\frac{\bar{c}}{2V_0}$, as is common in English literature.

$$Z_\alpha = -\frac{V_0 F \rho}{2m}\left[C_{L\alpha} + C_{D|0}\right] \tag{7}$$

$$M_q = \frac{F\rho\bar{c}^2 V_0}{4I_{yy}} C_{mq} \tag{8}$$

$$M_\alpha = \frac{V_0^2 F\rho\bar{c}}{2I_{yy}} C_{m\alpha} \tag{9}$$

From equ. 7 to equ. 9 already, a proportional dependency of all values on the trimmed airspeed V_0 becomes apparent. As a consequence, a more pronounced coupling between Short Period mode and Phugoid in flight phases at the lower end of the airspeed range can be expected. This relation is especially detrimental in the landing approach, during which airspeed is typically gradually reduced in preparation for touch-down and accurate altitude tracking is crucial for safe operation.

3.2 Estimation of Longitudinal Dynamics using a Handbook Method.

Aircraft designers favor handbook methods due to their simplicity, therefore the handbook method of Quabeck [7] is applied for it is utilized in the Institute's UAV design tool [25]. The method allows the determination of the neutral point of wing and tail combinations as well as estimation methods for the static stability in longitudinal and lateral motion. The calculations are implemented in *Microsoft Excel 2013* and the implementation validated using an example given in [7]. The procedure is outlined in the following.

3.2.1 Neutral Point Estimation Using the Rectangular Substitute Wing Method

An arbitrary, symmetrical wing plan-form with half span s is approximated by a number n trapezoids, for which a rectangular substitute wing of identical wing area F and neutral point coordinate $x_{N,W}$ is defined. The rectangular substitute wing is described by the substitute wing half-span s_E, substitute wing chord l_E and substitute wing leading edge coordinate x_{0E}. The approach is exemplified in the following Fig. 3, note that only one half-span is depicted.

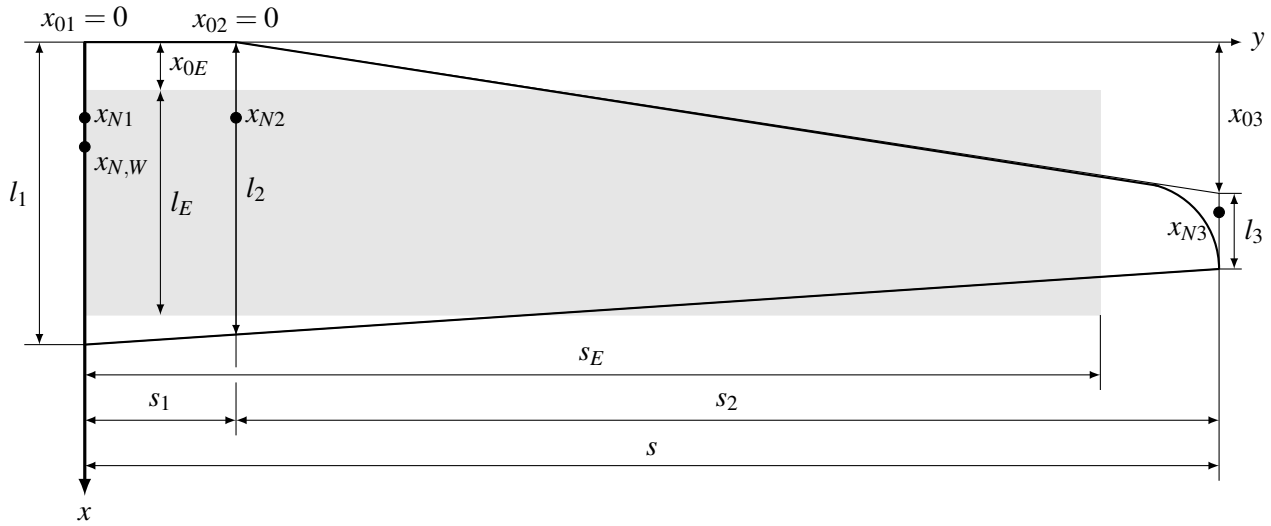

Figure 3 – Wing outline (solid line) and rectangular substitute wing (shaded area) with key features.

The wing area F is calculated by summing the areas of the number n trapezoids of span s_i featuring an inner/ outer chord length l_i and l_{i+1}, multiplied by a factor of 2 accounting for the second wing half:

$$F = 2\sum_{i=1}^{n} \frac{s_i}{2}(l_i + l_{i+1}) \tag{10}$$

The substitute wing leading edge coordinate x_{0E} is calculated as

$$x_{0E} = \frac{1}{3F}\sum_{i=1}^{n} s_i(x_{0i}(2l_i + l_{i+1}) + x_{0i+1}(l_i + 2l_{i+1})) \tag{11}$$

Assuming a symmetrical wing plan-form and the fulfillment of the condition $c_a(y) \equiv c_A$, which is reasoned to be given in case of an identical profile over the entire span of the wing, the substitute wing chord l_E is calculated as follows:

$$l_E = \frac{1}{F}\int_{-s}^{s} l^2(y)dy = \frac{2}{F}\int_{0}^{s} l^2(y)dy \tag{12}$$

with $l(y)$ being the chord length over the wingspan, and the wing area F. Applying the approximation by trapezoids, the integral to calculate the substitute wing chord length l_E can subsequently be replaced by a sum:

$$l_E = \frac{2}{3F}\sum_{i=1}^{n} s_i(l_i^2 + l_i l_{i+1} + l_{i+1}^2) \tag{13}$$

The coordinate of the neutral point $x_{N,W}$ is finally calculated as

$$x_{N,W} = x_{0E} + \frac{l_E}{4} \tag{14}$$

Alternatively, the neutral point $x_{N,W}$ of the substitute wing can be calculated directly as

$$x_{N,W} = \frac{1}{3F}\sum_{i=1}^{n} s_i(x_{Ni}(2l_i + l_{i+1}) + x_{Ni+1}(l_i + 2l_{i+1})) \tag{15}$$

Aforementioned relations can also be applied to asymmetrical wing plan-forms, which is typically the case for vertical stabilizers, if the integration limits/ the factors before the sums respectively are adjusted accordingly. The relations for wing area F, leading edge coordinate x_{0E} and substitute wing chord l_E change correspondingly:

$$F_V = \sum_{i=1}^{n} \frac{s_i}{2}(l_i + l_{i+1}) \tag{16}$$

$$x_{0E,V} = \frac{1}{6F}\sum_{i=1}^{n} s_i(x_{0i}(2l_i + l_{i+1}) + x_{0i+1}(l_i + 2l_{i+1})) \tag{17}$$

$$l_{E,V} = \frac{1}{3F}\sum_{i=1}^{n} s_i(l_i^2 + l_i l_{i+1} + l_{i+1}^2) \tag{18}$$

3.2.2 Neutral Point and Static Margin of a Wing - Tail - Configuration

The neutral point x_N of the wing-tail-configuration can be calculated by adding a coordinate shift Δx_N, which is caused by the horizontal stabilizer, to the coordinate of the wing neutral point $x_{N,W}$:

$$x_N = x_{N,W} + \Delta x_N \tag{19}$$

After the position of the neutral point of the horizontal stabilizer $x_{N,H}$ is determined using the relations described in chapter 3.2.1, the coordinate shift Δx_N is finally calculated as

$$\frac{\Delta x_N}{l_E} = \frac{a_W a_H \frac{F_H}{F}}{\kappa_W + a_W a_H \frac{F_H}{F}} \frac{r_0}{l_E} \tag{20}$$

using the substitute wing chord l_E, the reference areas of wing and horizontal stabilizer F and F_H, and the distance between the aircraft's Center of Gravity (C.G.) and the neutral point of the horizontal stabilizer r_0. The aspect ratio factors of wing and tail a_W and a_H are calculated as follows:

$$a_{W/H} = \frac{\Lambda_{W/H}}{\sqrt{\Lambda_{W/H}^2 + 4} + 2} \tag{21}$$

with the aspect ratio $\Lambda_W = \frac{b^2}{F}$ using the wing span b and wing area F, F_H of wing and horizontal stabilizer respectively.
The downwash-factor κ_W takes the effect of the down-wash of the wing into account, it is defined as:

$$\kappa_W := \frac{\Lambda_W^2}{\left(\sqrt{\Lambda_W^2+4}+2\right)\left(\sqrt{\Lambda_W^2+4}-2\left(\left(\frac{4}{\pi}\right)^2-1\right)\right)} \tag{22}$$

The static margin σ can subsequently calculated as:

$$\sigma = \frac{x_N - x_{C.G.}}{l_E} \tag{23}$$

3.2.3 Coefficients of the Longitudinal Motion

A more detailed approach to the longitudinal dynamics is presented in [8]. The Short Period mode is modeled as an attenuated pitch oscillation around the C.G., applying the following characteristic polynomial:

$$I_{yy}\lambda^2 - \overline{M}_{\dot{\alpha},Qu}\lambda - M_{\alpha,Qu} = 0 \tag{24}$$

Equation 24 can be expanded into equ. 25 in order to express the relation by the use of aerodynamic coefficients, flight condition and design fundamentals:

$$I_{yy}\lambda^2 - \frac{\overline{c}}{V}\left(C_{m,\dot{\alpha}} + C_{m,\omega_y}\right)\overline{q}F\overline{c}\lambda - C_{m,\alpha}\overline{q}F\overline{c} = 0 \tag{25}$$

Analogue to equ. 4 and 5, the current method calculates the eigen-frequency of the Short Period mode $\omega_{0,SP,Qu}$ and its damping $\sigma_{SP,Qu}$ as follows:

$$\omega_{0,SP,Qu} = \sqrt{-\frac{1}{I_{yy}}C_{m,\alpha}\overline{q}F\overline{c}} \tag{26}$$

$$\sigma_{SP,Qu} = -\frac{1}{2I_{yy}}\frac{\overline{c}}{V_0}\left(C_{m,\dot{\alpha}} + C_{m,\omega_y}\right)\overline{q}F\overline{c} \tag{27}$$

By expanding the dynamic pressure $\overline{q}$, equ. 26 and 27 can be separated into a configuration specific term and the test point specific values of airspeed V_0 and air density ρ.

$$\omega_{0,SP,Qu} = \left(\sqrt{-\frac{1}{2I_{yy}}C_{m,\alpha}F\overline{c}}\right)\sqrt{\rho}V_0 \tag{28}$$

$$\sigma_{SP,Qu} = -\left(\frac{1}{4I_{yy}}\left(C_{m,\dot{\alpha}} + C_{m,\omega_y}\right)F\overline{c}^2\right)\rho V_0 \tag{29}$$

For the calculation of $C_{m\alpha}$ and $\left(C_{m,\dot{\alpha}} + C_{m,\omega_y}\right)$ the following relations are proposed:

$$C_{m\alpha} = 2\pi a_W^{\times}\frac{x_{C.G.} - x_{N,W}}{\overline{c}} + \left(1 - \frac{\delta\alpha_W}{\delta\alpha}\right)2\pi a_H^{\times}\frac{\overline{q_H}}{\overline{q}}\frac{F_H}{F}\frac{r_0}{\overline{c}} \tag{30}$$

$$C_{m\alpha} = 2\pi a_W a_{p,W}(\alpha)\frac{x_{C.G.} - x_{N,W}}{\overline{c}} + \left(1 - \frac{4a_W a_{p,W}(\alpha)}{\Lambda}\right)2\pi a_H a_{p,H}(\alpha)\frac{\overline{q_H}}{\overline{q}}\frac{F_H}{F}\frac{r_0}{\overline{c}} \tag{31}$$

$$C_{m,\dot{\alpha}} + C_{m,\omega_y} \approx -2\pi a_H^{\times}\frac{F_H}{F}\frac{r_0^2}{\overline{c}^2}\left(1 + \frac{\delta\alpha_W}{\delta\alpha}\right) \approx -2\pi a_H a_{p,H}(\alpha)\frac{F_H}{F}\frac{r_0^2}{\overline{c}^2}\left(1 + \frac{4a_W a_{p,W}(\alpha)}{\Lambda}\right) \tag{32}$$

The factors $a_{p,W}$ and $a_{p,H}$ account for an increase of the lift slope coefficients $C_{LW,\alpha}$ and $C_{LH,\alpha}$ of wing and horizontal stabilizer due to viscous effects at Reynolds-numbers below 10^6 and can be set to 1 in a suitable approximation.
A comparison of equ. 3 and 24 as well as their coefficients shows, that equ. 3 can be transformed into equ. 24 by setting the state-space parameter Z_α to 0 and $C_{mq} = C_{m,\dot{\alpha}} + C_{m,\omega_y}$. The latter step is

possible, since both aerodynamic coefficients describe a moment due to an angular motion around the pitching axis of the aircraft. The coefficient estimates presented in equ. 32 to 31 are therefore also applied for the estimation of the state-space parameters as presented in equ. 7 to 9. In order to account for the state-space parameter Z_α, the coefficients $C_{L,\alpha}$ and $C_{D|0}$ can be estimated according to the following equations:

$$C_{L,\alpha} = 2\pi a_W a_{p,W}(\alpha) + 2\pi a_H a_{p,H}(\alpha) \left(1 - \frac{4 a_W a_{p,W}(\alpha)}{\Lambda}\right) \frac{\overline{q_H}}{\overline{q}} \frac{F_H}{F} \tag{33}$$

$$C_{D|0} = C_{D0} + k C_{L|0}^2 \tag{34}$$

3.3 AVL Simulation

For simulation the software *Athena Vortex Lattice 3.37* (AVL) Version 3.37 [23, 26] is being used. The software is selected due to its code maturity and command line interface that facilitates automation using Jupyter notebooks [27]. Aerodynamic coefficients as well as frequency and damping of eigenmodes are determined using different input geometry (see Fig. 4) and vortex lattice method to determine aerodynamic forces and moments in combination with the mass properties of the UAV scrutizined.

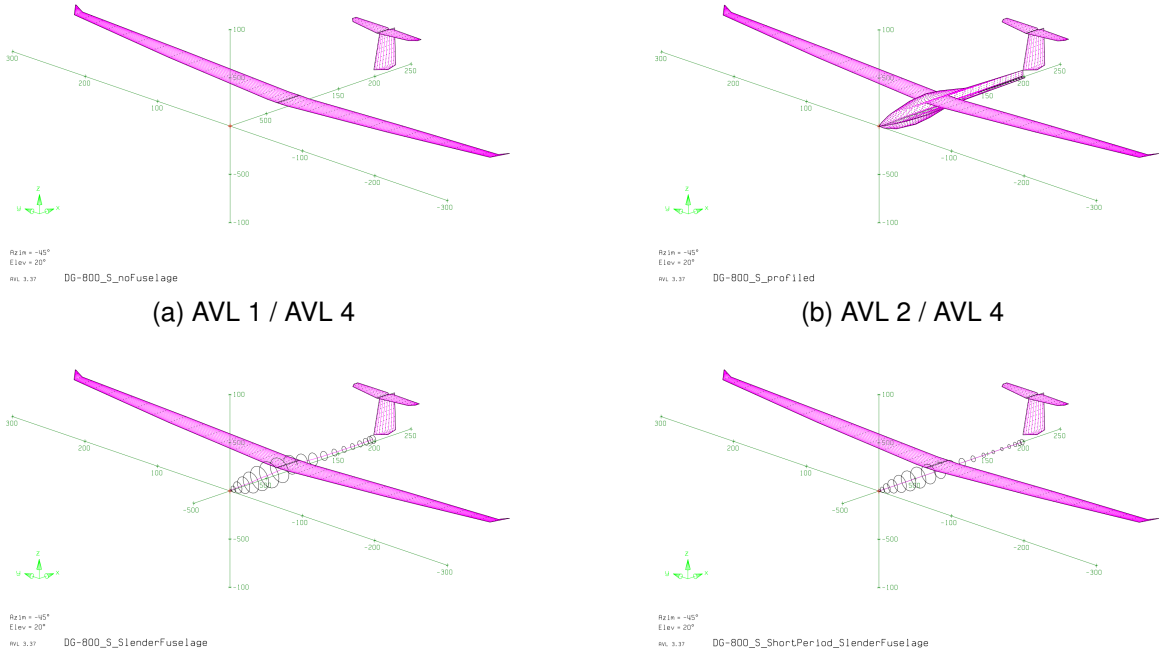

(a) AVL 1 / AVL 4

(b) AVL 2 / AVL 4

(c) AVL 3 DR / AVL 6 DR

(d) AVL 3 SP / AVL 6 SP

Figure 4 – Representations of the geometric configurations used for simulation in *AVL 3.37*, see also Table 3.

In order to assess the effects of different design features in the prediction of dynamic properties, eigenmode simulations are conducted with different geometric features as inputs. The level of detail of simulation input geometry is increased, resembling the increasing amount of knowledge of an aircraft in the course of its design process. For the fuselage, three different models are considered: A cross-fuselage representation and two slender-body representations. The cross-fuselage models the fuselage as aerodynamic surfaces in the xy- and xz-plane, that represent the side- and top-view of the fuselage (Fig. 4b). The slender bodies are described by circular sections, which diameters and position are determined by the either the fuselage's side-view (Fig. 4c) or the fuselage's top-view (Fig. 4d) as used in the cross-fuselage representation. Since the fuselage's cross-sections feature the egg-shape typical for the fuselage of sailplanes, this results in a slimmer slender body derived from the top-view than from the side-view. Since the slender body derived from the side-view is

considered more relevant for the lateral motion, respective configurations are denoted with the abbreviation *DR*. Configurations incorporating the slender body derived from the top-view are indicated by the abbreviation *SP*. The configurations with considered features are summarized in the following Table 3.

Table 3 – Geometric configurations and geometric input features.

Configuration	*Wing Profile*	*Stabilizer Profile*	*Fuselage*	*Figure*
AVL 1	None	None	None	Fig. 4a
AVL 2	None	None	Cross fuselage	Fig. 4b
AVL 3 DR	None	None	Slender body (side-view)	Fig. 4c
AVL 3 SP	None	None	Slender body (top-view)	Fig. 4d
AVL 4	HQ/W 2.5/15	NACA 0009	None	Fig. 4a
AVL 5	HQ/W 2.5/15	NACA 0009	Cross fuselage	Fig. 4b
AVL 6 DR	HQ/W 2.5/15	NACA 0009	Slender body (side-view)	Fig. 4c
AVL 6 SP	HQ/W 2.5/15	NACA 0009	Slender body (top-view)	Fig. 4d

3.4 Method of Comparison

In order to compare the different estimates of frequency ω_{SP} and damping σ_{SP} of the Short Period mode, the respective values are calculated and compared by plotting them on a pole-zero map. For the handbook methods the geometric data as provided in Tables 5 to 7 is implemented. The AVL-simulations employ more detailed data in the comparably small regions at the wingtips and at the wing-fuselage fairings. The values for trimmed airspeed V_0 and air density ρ are chosen to match the flight test data [4]. *AVL 3.37* provides the values of frequency ω_{SP} and damping σ_{SP}, as well as aerodynamic coefficients as a simulation result that are used as they are. In case of the estimates using handbook methods described in chapters 3.1 and 3.2, the frequency ω_{SP} and damping σ_{SP} for each velocity are calculated according to three different procedures as listed below. A more detailed summary including all relations is given in chapter A.1 in the appendix.

- M1: Equ. 4 and 5 for frequency ω_{SP} and damping σ_{SP}, using the averaged identified values for aerodynamic coefficients (Tab. 2) as presented in [4].
- M2: Equ. 26 and 27 for frequency $\omega_{SP,Qu}$ and damping $\sigma_{SP,Qu}$, using the estimates of aerodynamic coefficients according to equ. 31 and 32.
- M3: Equ. 4 and 5 for frequency ω_{SP} and damping σ_{SP}, using the estimates of aerodynamic coefficients of equ. 31, 32, 33, and 34 as proposed by Quabeck [7, 8].

4. Results and Discussion

The results of the estimates are compiled in the following Fig. 5, which represents a sub-section of the pole-zero map presented in Fig. 2. Values of the damping σ_{SP} are represented on the x-axis, values of frequency ω_{SP} on the y-axis.

Even though the flight test points (blue dots) exhibit considerable scatter, the estimates of method M1 (blue dashed line with squares) for frequency ω_{SP} and damping σ_{SP} lie in the region of estimates of methods M3 and AVL 1 to AVL 6 DR. This indicates that the errors of the flight test points, by and large, cancel out when averaged. In the following, all estimates will be compared to the estimates of method M1.

In terms of damping σ_{SP} all but method M2 (black dashed line with squares) provide estimates in the region of method M1. It is noteworthy, however, that all predictions overestimate the damping σ_{SP}. The estimates of method M2 predicts values of about half the values of M1 (compare values for the damping σ_{SP} on the x-axis). Of the remaining methods, the lowest values in terms of damping σ_{SP} are predicted by the simulations AVL 2 and AVL 5, which come also closest to the values of method M1. The estimates for frequency ω_{SP} deviate in a larger extent from the values of method M1. In this

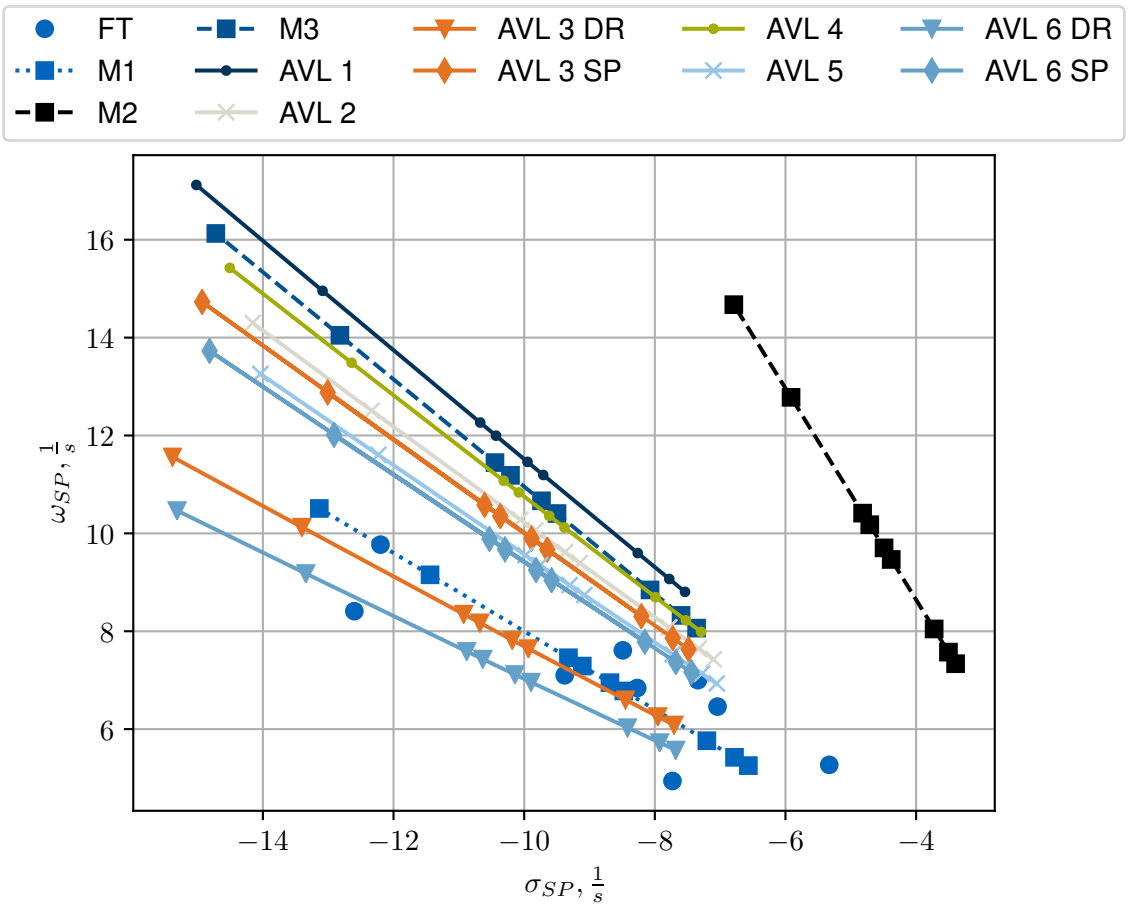

Figure 5 – Comparison of estimation results (handbook methods dashed lines with squares, *AVL* simulations without fuselage representation solid lines and dots, *AVL* simulation including fuselage representation with solid lines and crosses/triangles) for the frequency ω_{SP} and damping σ_{SP} with flight test results (dots).

regard, the estimates of method M2 are larger than the estimates of method M1 and approximately in the mid of the estimate range provided by the remaining methods (compare values for the frequency ω_{SP} on the y-axis). Method M3 (dark blue dashed line with squares), that in contrast of method M2 accounts for all terms in equ. 3, predicts larger values for frequency ω_{SP} and is in good agreement with the estimates of *AVL 3.37* simulations AVL 1 and AVL 4 (solid lines with dots) that were provided the wing geometry without/with specified airfoils, yet no representation of the fuselage (see Table 3 and Fig. 4). The simulation estimates featuring a cross-fuselage AVL 2 and AVL 5 (solid lines with crosses) are larger than estimates of M1, while smaller than the simulations without fuselage representation AVL 1 and AVL 4. The values predicted by the simulations AVL 3 SP and AVL 6 SP (solid lines with diamonds), that model the fuselage as a slender body based on the top-view, are close to the predictions of AVL 2 and AVL 5, with larger predicted values for the damping σ_{SP} as well as frequency ω_{SP}. The simulations AVL 3 DR and AVL 6 DR (solid lines with triangles), that model the fuselage as a slender body based on the dimensions of the side-view, also predict larger values for the frequency ω_{SP} than method M1, but are in best agreement with method M1 in this regard.

In order to assess the accuracy of predictions concerning the aerodynamic coefficients involved in the Short Period mode according to equ. 3 to 9, namely $\left[C_{L\alpha}+C_{D|0}\right]$, C_{mq} and $C_{m\alpha}$, the respective values are presented in Fig. 6. Each value predicted by the methods M2 and M3, as well as AVL 1 to AVL 6 are normalized using the value of each aerodynamic coefficient as identified from flight test data (see Tab. 2). The 95%-confidence interval is indicated by the black lines of the bars representing the values of methods FT/M1.

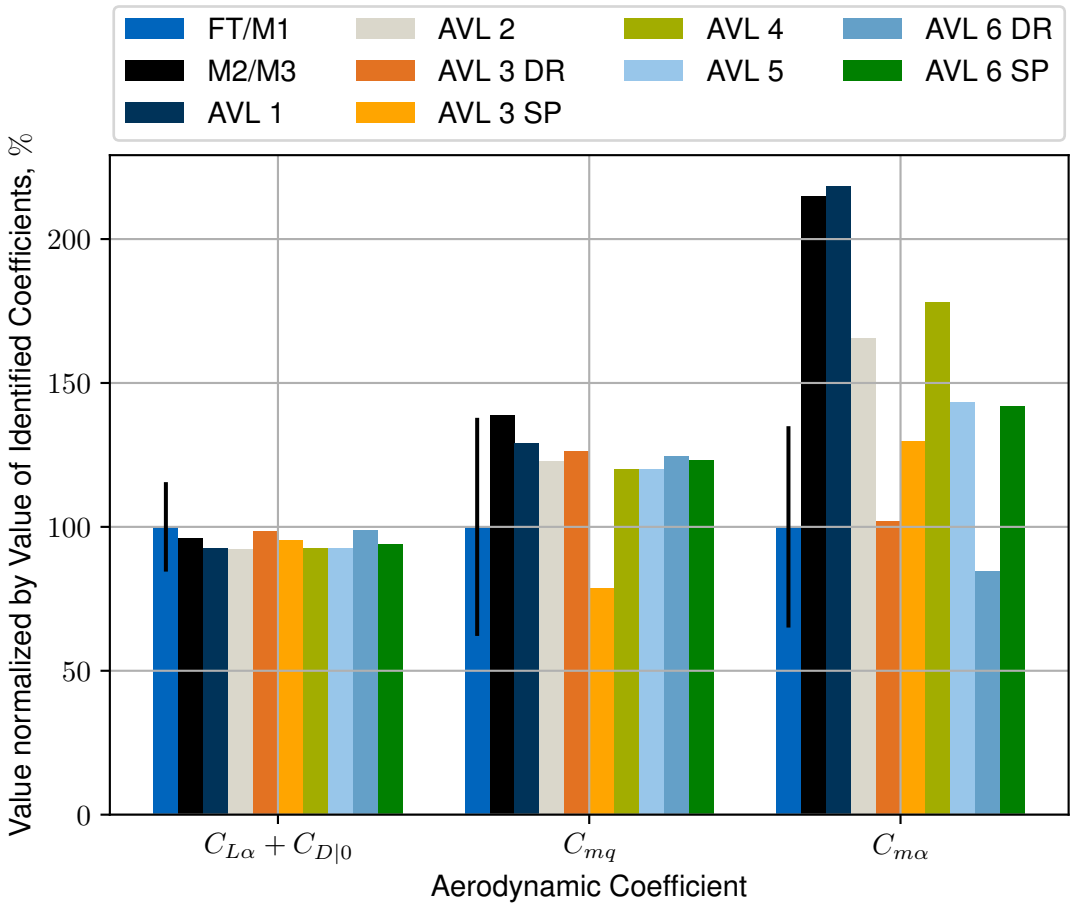

Figure 6 – Comparison of predicted values of aerodynamic coefficients, normalized to identified values from flight test data and 95%-confidence intervals (see Tab. 2).

For all methods, the values of the aerodynamic coefficient $\left[C_{L\alpha} + C_{D|0}\right]$ lie within a range of 90% of the value identified from flight test data. It is noteworthy, that all methods predict lower values than the averaged identified value, even though every prediction is well within the 95%-confidence interval.
Except for simulation AVL 3 SP, the predictions of the aerodynamic coefficient C_{mq} are greater than the averaged identified value. Also the influence of the fuselage representations in the simulations is not as profound, since the value is predominantly influenced by the distance of the neutral point of the horizontal stabilizer from the C.G. r_0 (compare quadratic relation in equ. 32). In this regard, the large deviation of about 20% for simulation AVL 3 SP is unexpected and cannot be explained conclusively to date, especially when regarding the predicted value of simulation AVL 6 SP, that aligns well with the other predictions.
The largest differences can be found for the predicted values of the aerodynamic coefficient $C_{m\alpha}$: The values range from about 80% for the simulation AVL 6 DR to more than 200% for AVL 1. The largest values are predicted by the handbook method(s) M2/M3 (equ. 30 and equ. 31 respectively) and the simulation AVL 1. Neither of aforementioned methods account for the destabilizing influences of the fuselage, which leads to an over-estimation of predicted values of about 100%. The lowest values for the aerodynamic coefficient $C_{m\alpha}$ are predicted by the simulations AVL 3 DR and AVL 6 DR, that feature a slender body representation (side-view) of the fuselage. For explaining the differences between the simulations AVL 1 and AVL 4, AVL 2 and AVL 5, as well as AVL 3 DR and AVL 6 DR, a consideration of the different airfoil lift slopes seems obvious, since the airfoil lift slope default to 2π if no airfoil is specified and decreases, as soon as an airfoil is assigned, leading to smaller values of the aerodynamic coefficient $C_{m\alpha}$. It needs to be pointed out, however, that the difference between simulations AVL 3 SP and AVL 6 SP does not follow this rationale.
The large deviations between simulations AVL 3 DR/AVL 3 SP and AVL 6 DR/AVL 6 SP can be ex-

plained by the overall larger fuselage diameter. Also, the similarity of results between simulations AVL 5 (featuring a cross fuselage) and AVL 6 SP (slender body representation, sideview) is noteworthy.

5. Conclusion

Investigations aimed at the estimation of the frequency ω_{SP} and damping σ_{SP} of the Short Period mode of an UAV using data typically available in early design stages, namely planform and position of aerodynamic surfaces, airfoils, fuselage shape, and mass moment of inertia. The data was used as input for two different handbook methods and a total of six vortex-lattice simulations using the program *AVL 3.37*. Results from flight tests with one UAV in the range of linear aerodynamics served as a reference.

Results show, that the prediction of the characteristics of the Short Period mode based on design data is feasible. While the simplest handbook method M2 underestimates the damping σ_{SP} by a factor of about 2, its predictions concerning the frequency of the Short Period mode ω_{SP} are in a reasonable range. The underestimation of the damping σ_{SP} can be mitigated by considering all terms in the characteristic equation 3 using handbook estimates for the influencing aerodynamic coefficients (method M3). The resulting estimates lie in between the estimates provided by the simplest vortex-lattice simulations AVL 1 and AVL 4, that only account for planform and position of aerodynamic surfaces (i.e. wing and horizontal stabilizer), and in case of AVL 4 for airfoils. The effect of the airfoils is typically a reduction of predicted values of both frequency ω_{SP} and damping σ_{SP}. When the fuselage is considered by either intersecting aerodynamic surfaces resembling the fuselages side- and top-view (cross-fuselage, AVL 2/AVL 5) or slender bodies defined by the dimensions of the fuselage's side- (AVL 3 DR/AVL 6 DR) and top-view (AVL 3 SP/AVL 6 SP), the estimated values for the frequency ω_{SP} are reduced. Of the two different methods of fuselage representation, the inclusion of the fuselage as a slender body showed largest effects in terms of a reduction of frequency ω_{SP}. Flight test results are grouped between the vortex-lattice simulations considering the fuselage, with the simulations using a cross-representation on the upper and the simulations using a slender body (AVL 3 DR and AVL 6 DR) with the largest dimensions on the lower end of the range of frequency ω_{SP}. Results indicate, that the influence of the selected airfoil on overall dynamics is smaller than the influence of the fuselage, which in this case proved to have considerable destabilizing effect. Here, the usage of the vortex-lattice simulation tool *AVL 3.37* proved to be advantageous for the assessment of effects introduced by the fuselage, especially if a cross-fuselage representation is being implemented since one model can be used for the analysis of longitudinal and later lateral motion while results are comparable to results attained when using slender body representations. A subsequent estimation of the effect using the estimation method proposed by Raymer/NACA TR711 [28] also yielded a reduction the value's amount for the aerodynamic coefficient $C_{m\alpha}$ of about 35%, which brings the predicted value for $C_{m\alpha}$ of the handbook methods M2/M3 within 10% of the predicted value of simulation AVL 2 (cross-fuselage, no profile).

It needs to be stated, that the study is based on a reference data set limited to one configuration and to a number of nine test points which results feature rather high standard deviations. The averaged identified values of the aerodynamic coefficients $\left[C_{L\alpha} + C_{D|0}\right]$ and C_{mq}, however, are, by and large, within the 95%-confidence interval of the values identified experiment data. The averaged identified value of the aerodynamic coefficient $C_{m\alpha}$, on the other hand, differ to such scale, that an explanation of differences solely by statistical effects is deemed unlikely. Considering that the scrutinized UAV is a scaled model of a sailplane, which typically feature a fuselage designed to minimize its aerodynamic effect even though a comparably large portion of the top-view and side-view area is in front the C.G., the results suggest that the fuselage should be accounted for in the aerodynamic analysis of a design process.

6. Outlook

Since the coupling between Short Period mode and Phugoid mode is expected to be more pronounced at lower airspeeds V due to lower frequency ω_{SP} and damping σ_{SP}, future work will focus on the collection of flight test data at lower airspeeds V in order to assess presented estimation methods.

Since non-linear aerodynamics effects increase at lower airspeed V, further simulation implications are expected in this region. The accuracy of flight test results will be scrutinized in more detail in order to identify regions of confidence for frequency ω_{SP} and damping σ_{SP}.
Future flight test will also focus different UAVs, such as the FLEXOP flight demonstrator [2] and the HORYZN Silencio γ [29] eVTOL UAV in order to provide additional reference data for the methodology presented.

7. Contact Author Email Address

Sebastian.Koeberle@tum.de

8. Copyright Statement

References

[1] Sobron, A, Lundström, D and Krus, P. A Review of Current Research in Subscale Flight Testing and Analysis of Its Main Practical Challenges. *Aerospace*. Vol. 8, No. 3, p. 74. 2021. https://doi.org/10.3390/aerospace8030074.

[2] Stahl, P, Sendner, FM, Hermanutz, A, Rößler, C and Hornung, M. Mission and Aircraft Design of FLEXOP Unmanned Flying Demonstrator to Test Flutter Suppression within Visual Line of Sight. *17th AIAA Aviation Technology, Integration, and Operations Conference 2017*. Curran Associates Inc, Red Hook, NY, 2017. p. 11. https://doi.org/10.2514/6.2017-3766.

[3] Sobron, A, Lundström, D, Larsson, R, Krus, P and Jouannet, C. Methods for Efficient Flight Testing and Modelling of Remotely Piloted Aircraft within Visual Line-Of-Sight. *ICAS 2018*. The International Council of the Aeronautical Sciences c/o Deutsche Gesellschaft für Luft- und Raumfahrt, 2018. p. 11. URL http://www.diva-portal.org/smash/record.jsf?pid=diva2%3A1295432&dswid=-149.

[4] Koeberle, SJ, Albert, AE, Nagel, LH and Hornung, M. Flight Testing for Flight Dynamics Estimation of Medium-Sized UAVs. *AIAA Scitech 2021 Forum*. 2021. p. 1526. https://doi.org/10.2514/6.2021-1526.

[5] Chudoba, B. *Stability and Control of Conventional and Unconventional Aerospace Vehicle Configurations: A Generic Approach from Subsonic to Hypersonic Speeds*. Springer Aerospace Technology. Springer International Publishing, 2019.

[6] Sarojini, D, Harrison, E and Mavris, DN. Dynamic Environment for Loads Prediction and Handling Investigation (DELPHI). *AIAA Scitech 2021 Forum*. American Institute of Aeronautics and Astronautics, Reston, Virginia, 01112021. p. 2651. https://doi.org/10.2514/6.2021-0326.

[7] Quabeck, H. *Design, Leistung und Dynamik von Segelflugmodellen: Flugmechanische und aerodynamische Grundlagen und ihre praktische Nutzanwendung ; dynamische Aufgabenstellungen aus der Flugpraxis mit zahlreichen Beispielen*. 1st ed.. HQ-Modellflugliteratur, Babenhausen, 1994.

[8] Quabeck, H. *On the Longitudinal Stability of Gliders*. Online: http://www.hq-modellflug.de/theory%20contributions/longitudinal_flight_stability.pdf„ 2007

[9] Cooper, GE and Harper, RP. *The Use of Pilot Rating in the Evaluation of Aircraft Handling Qualities*. , 1969 URL https://ntrs.nasa.gov/archive/nasa/casi.ntrs.nasa.gov/19690013177.pdf.

[10] Pontzer, AE, Lower, MD and Miller, JR. *Unique aspects of flight testing unmanned aircraft systems: Aspects particuliers des essais en vol des aéronefs sans pilote*. AC/323(SCI)TP, Vol. 299. NATO Research & Technology Organisation, Neuilly-sur-Seine, 2010.

[11] Martinez Perez, M and Lowenberg, MH. Eigenvector similarity metrics for the identification and quantitative study of aircraft dynamic modes. *AIAA Scitech 2021 Forum*. 2021. p. 1724. https://doi.org/10.2514/6.2021-1724.

[12] Nguyen, DH, Lowenberg, MH, Neild, SA and Richardson, TS. Flying qualities assessment using nonlinear frequency response analysis. *AIAA Scitech 2021 Forum*. American Institute of Aeronautics and Astronautics, Reston, Virginia, 01112021. p. 337. https://doi.org/10.2514/6.2021-0759.

[13] Wiedemann, F. DG 800 S: Instruction Manual. , 2014. URL https://carf-models.com/files/product/6d/bd/26/manual_carf_dg-800s.pdf.

[14] Luis de Magalhães Ross, Victor. Instrumentation and Flight Testing of a UAV of type DG-800 S. Instrumentierung und Flugerprobung eines unbemannten Fluggeraätes des Typ DG-800 S. Bachelor's Thesis. Technical University of Munich. Munich, 2020.

[15] Nagel, L. Instrumentation and Flight Testing of a UAV of Type DG-800 S. Bachelor's Thesis. Technical University of Munich. Munich, 02.11.2020.

[16] P100-RX - JetCat. , 2020. URL https://www.jetcat.de/en/productdetails/produkte/jetcat/produkte/hobby/Engines/p100_rx.

[17] Koeberle, SJ, Rumpf, M, Scheufele, B and Hornung, M. Design of a Low-Cost RPAS Data Acquisition System for Education. *AIAA Aviation 2019 Forum*. American Institute of Aeronautics and Astronautics, Reston, Virginia, 06172019. p. 3658. https://doi.org/10.2514/6.2019-3658.

[18] Creaform. MaxSHOT 3D Handheld Optical Coordinate Measuring System | Creaform. , 2021. URL https://www.creaform3d.com/en/metrology-solutions/optical-measuring-systems-maxshot-3d.

[19] Creaform. HandySCAN 3D | SILVER Series: Professional 3D Laser Scanners. , 2021. URL https://www.creaform3d.com/en/handyscan-3d-silver-series-professional-3d.

[20] Creaform. 3D Software Platform and Application Suite | Creaform. , 2021. URL https://www.creaform3d.com/en/metrology-solutions/3d-applications-software-platforms.

[21] Çetin, KM. Development and Implementation of a 3D-Scanning-Tool-Chain for the Characterization of UAVs. Bachelor's Thesis. Technical University of Munich. Munich, 06.04.2020.

[22] van Brügge, L. Development and Implementation of a 3D-Scanning-Toolchain for the Geometric Characterization of UAVs. Bachelor's Thesis. Technical University of Munich. Munich, 31.10.2020.

[23] Drela, M and Youngren, H. AVL: Aerodynamic Analysis, Trim Calculation, Dynamic Stability Analysis, Aircraft Configuration Development. , 23.02.2017. URL http://web.mit.edu/drela/Public/web/avl/.

[24] Brockhaus, R. *Flugregelung*. zweite, neu bearbeitete auflage ed.. Springer, Berlin and Heidelberg, 2001. https://doi.org/10.1007/978-3-662-07264-6.

[25] Rößler, C. *Conceptual Design of Unmanned Aircraft with Fuel Cell Propulsion System: Zugl.: München, Techn. Univ., Diss., 2012*. 1st ed.. Luftfahrt. Verl. Dr. Hut, München, 2012.

[26] Drela, M. *Flight Vehicle Aerodynamics*. MIT Press, Cambridge, Mass. [u.a.], 2014.

[27] Project Jupyter. , 2021. URL https://jupyter.org/.

[28] Raymer, DP. *Aircraft Design: A Conceptual Approach*. sixth edition ed.. AIAA education series. American Institute of Aeronautics and Astronautics Inc, Reston, VA, 2018.

[29] Nagy, B. The Aircraft - HORYZN - Prototyping the Aerospace of Tomorrow. , 2020. URL https://horyzn.org/silencio/.

Appendix

A.1 Detailed presentation of estimation methods M1 to M3.

Table 4 – Overview over the different methods of estimating frequency ω_{SP} and damping σ_{SP}.

M1: *Linearized, decoupled, reduced state-space model with identified coefficients.*

$$\omega_{0,SP} \approx \sqrt{Z_\alpha M_q - M_\alpha} \qquad Z_\alpha = -\frac{V_0 F \rho}{2m}\left[C_{L\alpha} + C_{D|0}\right] \qquad C_{L\alpha} + C_{D|0} = 6.5782$$
$$\sigma_{SP} \approx \tfrac{1}{2}(M_q + Z_\alpha) \qquad M_q = \frac{F\bar{q}\bar{c}^2}{2I_{yy}V_0} C_{mq} \qquad C_{mq} = -21.7515$$
$$\omega_{SP} = \sqrt{\omega_{0,SP}^2 - \sigma_{SP}^2} \qquad M_\alpha = \frac{V_0^2 F \rho \bar{c}}{2I_{yy}} C_{m\alpha} \qquad C_{m\alpha} = -0.5143$$

M2: *Handbook method as presented by Quabeck [8].*

$$\omega_{0,SP,Qu} \approx \sqrt{\frac{-M_{\alpha,Qu}}{I_{yy}}} \qquad M_{\alpha,Qu} = \overline{q} F \bar{c} C_{m,\alpha}$$
$$\sigma_{SP,Qu} \approx \frac{\overline{M}_{\dot{\alpha},Qu}}{2I_{yy}} \qquad \overline{M}_{\dot{\alpha},Qu} = \frac{\overline{q} F \bar{c}^2}{V_0}\left(C_{m,\dot{\alpha}} + C_{m,\omega_y}\right)$$
$$\omega_{SP,Qu} = \sqrt{\omega_{0,SP,Qu}^2 - \sigma_{SP,Qu}^2}$$
$$C_{m,\alpha} = 2\pi a_W a_{p,W}(\alpha)\tfrac{x_{C.G.} - x_{N,W}}{\bar{c}} + \left(1 - \tfrac{4a_W a_{p,W}(\alpha)}{\Lambda}\right) 2\pi a_H a_{p,H}(\alpha) \tfrac{\overline{q_H}}{\overline{q}} \tfrac{F_H}{F} \tfrac{r_0}{\bar{c}}$$
$$C_{m,\dot{\alpha}} + C_{m,\omega_y} = -2\pi a_H a_{p,H}(\alpha) \tfrac{F_H}{F} \tfrac{r_0^2}{\bar{c}^2}\left(1 + \tfrac{4a_W a_{p,W}(\alpha)}{\Lambda}\right)$$

M3: *Linearized, decoupled, reduced state-space model with estimated coefficients [7, 8]*

$$\omega_{0,SP} \approx \sqrt{Z_\alpha M_q - M_\alpha} \qquad Z_\alpha = -\frac{V_0 F \rho}{2m}\left[C_{L\alpha} + C_{D|0}\right]$$
$$\sigma_{SP} \approx \tfrac{1}{2}(M_q + Z_\alpha) \qquad M_q = \frac{F\bar{q}\bar{c}^2}{I_{yy}V_0}\left(C_{m,\dot{\alpha}} + C_{m,\omega_y}\right)$$
$$\omega_{SP} = \sqrt{\omega_{0,SP}^2 - \sigma_{SP}^2} \qquad M_\alpha = \frac{V_0^2 F \rho \bar{c}}{2I_{yy}} C_{m\alpha}$$
$$C_{m\alpha} = 2\pi a_W a_{p,W}(\alpha)\tfrac{x_{C.G.} - x_{N,W}}{\bar{c}} + \left(1 - \tfrac{4a_W a_{p,W}(\alpha)}{\Lambda}\right) 2\pi a_H a_{p,H}(\alpha) \tfrac{\overline{q_H}}{\overline{q}} \tfrac{F_H}{F} \tfrac{r_0}{\bar{c}}$$
$$C_{m\dot{\alpha}} + C_{m,\omega_y} = -2\pi a_H a_{p,H}(\alpha) \tfrac{F_H}{F} \tfrac{r_0^2}{\bar{c}^2}\left(1 + \tfrac{4a_W a_{p,W}(\alpha)}{\Lambda}\right)$$
$$C_{L\alpha} = 2\pi a_W a_{p,W}(\alpha) + 2\pi a_H a_{p,H}(\alpha)\left(1 - \tfrac{4a_W a_{p,W}(\alpha)}{\Lambda}\right) \tfrac{\overline{q_H}}{\overline{q}} \tfrac{F_H}{F}$$
$$C_{D|0} = C_{D0} + kC_{L|0}^2 \text{ with } k = 0.0122$$

A.2 List of Symbols

$a_{[]}$	=	Aspect ratio factor	$a_{p[]}$	=	Increase in lift slope coeff.
b	=	Wing span	$\bar{c}$	=	Reference chord length
$C_{[][]}$	=	Aerodynamic coefficient	$C_D\|_0$	=	Drag coefficient in trim point
$F_{[]}$	=	Aerodynamic surface Area	g	=	Gravitational constant
I_{yy}	=	Moment of inertia around y-axis	l_E	=	Substitute wing chord
l_i, l_{i+1}	=	Inner/outer chord length i$^{\text{th}}$ trap	$l(y)$	=	Wing chord over wingspan
m	=	Aircraft mass	q	=	Pitch rate
$\overline{q_{[]}}$	=	Dyn. pressure at wing/tail	r_0	=	Difference between $x_{C.G.}$ and $x_{N,H}$
s	=	Half span	s_E	=	Substitute wing half-span
s_i	=	Span of i$^{\text{th}}$ trapezoid	$s_{[]}$	=	Standard deviation
V, V_0	=	Airspeed, trimmed airspeed	$x_{C.G.}$	=	X-position Center of Gravity
x_{0E}	=	Subst. wing LE coordinate	x_{0i}	=	X-position of i$^{\text{th}}$ chord
x_N	=	X-pos. neutral point (a/c)	$x_{N,[]}$	=	X-pos. neutral point (e.g. wing)
x_{Ni}	=	X-pos. neutral point (chord)	Δx_N	=	Shift of neutral point
$\dot{[]}$	=	Derivative by time	α	=	Angle of attack
γ	=	Flight path angle	δ_T	=	Throttle
η	=	Elevator deflection	κ_W	=	Downwash factor
$\Lambda_{[]}$	=	Aspect ratio	ρ	=	Air density
σ	=	Static margin	$\sigma_{SP,[]}$	=	Short period damping
$\omega_{0,SP,[]}$	=	Short Period Frequency	ω_{SP}	=	Damped Short Period Frequ.

A.3 Geometric Data of the DG-800 S testbed.

Summary of geometric data of the DG-800 S testbed as implemented in the handbook method and *AVL* simulations presented.

Table 5 – Geometric data of the wing of UAV *CARF-Models Ltd.* DG-800 S.

Wing		
General Data		
Half span	b_{ref}	3000 mm
Reference Area	F	1332161 mm^2
Reference chord	$\overline{c}$	236 mm
Aspect Ratio	Λ	27.5
X-position		650 mm
Inner Trapezoid		
Span	s_1	1498 mm
Inner chord length	l_1	299 mm
Inner chord x-position	x_{01}	0 mm
Inner chord x-position neutralpoint	x_{N1}	74.75 mm
Outer chord	l_2	238 mm
Outer chord x-position	x_{02}	0 mm
Outer chord x-position neutralpoint	x_{N2}	59.5 mm
Outer Trapezoid		
Span	s_2	1495 mm
Inner chord length	l_2	238 mm
Inner chord x-position	x_{02}	0 mm
Inner chord x-position neutralpoint	x_{N2}	59.5 mm
Outer chord	l_3	115 mm
Outer chord x-position	x_{03}	68 mm
Outer chord x-position neutralpoint	x_{N3}	96.75 mm

Table 6 – Geometric data of the horizontal stabilizer of UAV *CARF-Models Ltd.* DG-800 S.

Horizontal Stabilizer		
Overall Data		
Half span		426 mm
Surface area	F_H	122678 mm^2
Aspect Ratio		1.48
X-position		2024 mm
Incidence angle		1.3°
Inner Trapezoid		
Span	s_1	32 mm
Inner chord length	l_1	163 mm
Inner chord x-position	x_{01}	0 mm
Inner chord x-position neutralpoint	x_{N1}	40.75 mm
Outer chord length	l_2	183 mm
Outer chord x-position	x_{02}	4.5 mm
Outer chord x-position neutralpoint	x_{N2}	50.25 mm
Middle Trapezoid		
Span	s_2	353 mm
Inner chord length	l_2	183 mm
Inner chord x-position	x_{02}	4.5 mm
Inner chord x-position neutralpoint	x_{N2}	50.25 mm
Outer chord length	l_3	114 mm
Outer chord x-position	x_{03}	55 mm
Outer chord x-position neutralpoint	x_{N3}	83.5 mm
Outer Trapezoid		
Span	s_3	41 mm
Inner chord	l_3	114 mm
Inner chord x-position	x_{03}	55 mm
Inner chord x-position neutralpoint	x_{N3}	83.5 mm
Outer chord length	l_4	51 mm
Outer chord x-position	x_{04}	113 mm
Outer chord x-position neutralpoint	x_{N4}	125.75 mm

Table 7 – Geometric data of the vertical stabilizer of UAV *CARF-Models Ltd.* DG-800 S.

Vertical Stabilizer		
Overall Data		
Span (in z-direction)	h_s	410 mm
Surface area	F_V	101056 mm^2
X-position		1983 mm
Lower Trapezoid		
Span	s_1	15 mm
Lower chord length	l_1	1 mm
Lower chord x-position	x_{01}	196 mm
Lower chord x-position neutralpoint	x_{N1}	196.25 mm
Upper chord length	l_2	168 mm
Upper chord x-position	x_{02}	134 mm
Upper chord x-position neutralpoint	x_{N2}	176 mm
Middle Trapezoid		
Span	s_2	32.4 mm
Lower chord length	l_2	168 mm
Lower chord x-position	x_{02}	134 mm
Lower section x-position neutralpoint	x_{N2}	176 mm
Upper chord length	l_3	301 mm
Upper chord x-position	x_{03}	0 mm
Upper chord x-position neutralpoint	x_{N3}	75.25 mm
Upper Trapezoid		
Span	s_3	362.6 mm
Lower chord length	l_3	301 mm
Lower section x-position	x_{03}	0 mm
Lower section x-position neutralpoint	x_{N3}	75.25 mm
Upper chord length	l_4	207.5 mm
Upper chord x-position	x_{04}	80.7 mm
Upper chord x-position neutralpoint	x_{N4}	132.6 mm

Table 8 – Geometric data of the fuselage of UAV *CARF-Models Ltd.* DG-800 S as used in AVL simulation in $[mm]$.

Cross Fuselage Data.				
Horizontal Fuselage Geometry (symmetric)				
Middle Section	0	0	0	1985
Section 1	50	29	0	1934
Section 2	150	59	0	870
Section 3	300	89	0	498
Section 4	550	107	0	1
Vertical Fuselage Geometry				
Section 1	647	0	172	1
Section 2	420	0	152	428
Section 3	164	0	89	1034
Section 4	117	0	71	1867
Section 5	37	0	32	1948
Section 6	14	0	14	1971
Section 7	0	0	0	1372
Section 8	69	0	-38	882
Section 9	242	0	-89	460
Section 10	502	0	-110	1

Slender Fuselage			
Top View		*Side View*	
1985	29	1984	71.3
1020	59	1199	89.3
798	89	951	133.5
543	107	848	151.9
300	89	702	166.3
150	59	647	171.7
50	29	502	159.1
0	1	420	151.9
50	-29	242	108.3
150	-59	164	89.2
300	-89	117	71.3
543	-107	69	47.7
798	-89	37	32
1020	-59	14	14
1985	-29	0	1
		14	-7.7
		37	-20.3
		69	-37.9
		117	-52
		164	-66
		242	-89
		420	-103
		502	-109.4
		647	-94.6
		702	-88.9
		848	-37.8
		951	-37.8
		1199	-25.1
		1984	-13.8